SCIENTIFIC REPORTS

OPEN

Large pinning forces and matching effects in $YBa_2Cu_3O_{7-\delta}$ thin films with $Ba_2Y(Nb/Ta)O_6$ nano-precipitates

Received: 16 July 2015
Accepted: 19 January 2016
Published: 18 February 2016

Lars Opherden[1,2,3], Max Sieger[1], Patrick Pahlke[1,2], Ruben Hühne[1], Ludwig Schultz[1,2], Alexander Meledin[4], Gustaaf Van Tendeloo[4], Rainer Nast[5], Bernhard Holzapfel[5], Marco Bianchetti[6], Judith L. MacManus-Driscoll[6] & Jens Hänisch[1,5]

The addition of mixed double perovskite $Ba_2Y(Nb/Ta)O_6$ (BYNTO) to $YBa_2Cu_3O_{7-\delta}$ (YBCO) thin films leads to a large improvement of the in-field current carrying capability. For low deposition rates, BYNTO grows as well-oriented, densely distributed nanocolumns. We achieved a pinning force density of 25 GN/m^3 at 77 K at a matching field of 2.3 T, which is among the highest values reported for YBCO. The anisotropy of the critical current density shows a complex behavior whereby additional maxima are developed at field dependent angles. This is caused by a matching effect of the magnetic fields *c*-axis component. The exponent *N* of the current-voltage characteristics (inversely proportional to the creep rate *S*) allows the depinning mechanism to be determined. It changes from a double-kink excitation below the matching field to pinning-potential-determined creep above it.

$YBa_2Cu_3O_{7-\delta}$ (YBCO) based coated conductors have large potential in such diverse applications as wires/cables, motors/generators, high-field coils, and superconducting permanent magnets, each of them with a certain range of temperature and magnetic field and a certain need in magnitude and isotropicity in critical current density J_c. In order to use the full potential of YBCO, it is mandatory to tailor its transport properties for the envisaged application. It is therefore necessary to understand how the critical current density J_c behaves over wide ranges of magnetic field strength H, temperature T and angle θ between H and the crystallographic c-axis. The $J_c(H,T,\theta)$ dependence, being determined by the underlying pinning landscape in a complex way[1], can be raised and adjusted by the creation of artificial defects within the superconductor which act as pinning centers. This can be achieved by e.g. irradiation[2], substrate decoration[3,4], rare-earth substitution[5,6], and incorporation of secondary phases. The latter one is relatively inexpensive and easy and therefore commonly used. After initial studies on naturally growing nanoparticles in YBCO thin films, such as Y_2O_3[7] (recently investigated again more closely as artificial pinning centers[8,9]), first investigations on artificial nanoparticles were made on $BaZrO_3$[10]. J_c could be strongly improved through incorporating this or related barium perovskites $BaMO_3$ (M transition metal) because they grow as globular or columnar structures which act as pinning centers. This has been reported for various techniques such as pulsed laser deposition (PLD)[11–15] or metal-organic chemical vapor deposition (MOCVD)[16]. In chemical deposition methods (CSD, MOD), usually randomly oriented, more or less isotropic nanoparticles are formed[17–19]. Secondary phases can furthermore introduce concurrent defects in the YBCO matrix. Strong positive correlations between nanostrain and J_c for example suggest that nanostrain and strain-induced defects such as stacking faults[20] or dislocations[21] act as pinning centers. Nanoinclusions of the double perovskites Ba_2YNbO_6 (BYNO) and Ba_2YTaO_6 (BYTO) have been suggested[22] as promising pinning centers due to several advantages compared to BZO. Nb or Ta ions are less likely to substitute for Y in YBCO, which should lead to a smaller T_c

[1]IFW Dresden, Institute for Metallic Materials, P.O. Box 270116, 01171 Dresden, Germany. [2]TU Dresden, Institute for Solid-State Physics, 01062 Dresden, Germany. [3]Dresden High Magnetic Field Laboratory (HLD-EMFL), Helmholtz-Zentrum Dresden-Rossendorf, 01328 Dresden, Germany. [4]University of Antwerp, EMAT Research Group, Groenenborgerlaan 171, 2020 Antwerp, Belgium. [5]KIT, Institute for Technical Physics, Hermann-von-Helmholtz-Platz 1, 76344 Eggenstein-Leopoldshafen, Germany. [6]University of Cambridge, Department of Materials Science and Metallurgy, 27 Charles Babbage Rd., Cambridge, CB3 0FS, UK. Correspondence and requests for materials should be addressed to L.O. (email: l.opherden@hzdr.de) or J. H. (email: jens.haenisch@kit.edu)

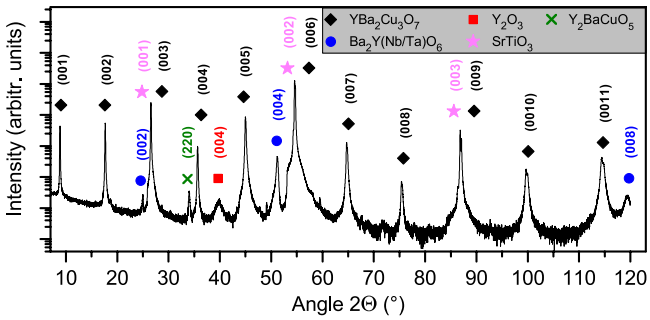

Figure 1. Θ-2Θ scan of the BYNTO:YBCO sample grown with $f_{Dep} = 1$ Hz. Co K_α was used for the measurement.

reduction[22], (a minute Nb substitution on Cu was even reported to slightly increase T_c[23]). Furthermore, according to their melting points (ZrO_2 2715 °C, Nb_2O_5 1512 °C and Ta_2O_5 1872 °C), Ta-O and Nb-O species presumably have a larger mobility on the substrate surface and within the film during growth than Zr-O, leading to well aligned BYNO nanocolumns[24,25] even at high deposition rates[26]. BYTO[27] and $Ba_2Y(Nb/Ru)O_6$[28] have been shown to form nanocolumns in PLD-grown films, whereas BYTO forms extended nanoparticles in CSD-grown films[29], very similar to the single perosvkites. Mixing BYNO and BYTO effectively adjusts interfacial energies and strain as well as diffusion lengths.

As shown by Ercolano *et al.*[30], double-doping of YBCO with BYNO and BYTO leads to a further improvement of the transport properties. Furthermore, these mixed-double perovskite $Ba_2Y(Nb/Ta)O_6$-doped YBCO films (BYNTO:YBCO) seem to show a more complex J_c anisotropy than single-doped samples. Related structures are the so-called 2411-phases, Cu-containing mixed double perovskites, which also were shown to improve J_c, however with less chemical stability and less tendency to form nanocolumns[31–33]. A deeper investigation of the material system BYNTO:YBCO is needed to provide a better understanding of its complex pinning landscape and the resulting effects on J_c (H,T,θ). This detailed study shows the influence of the microstructure of such BYNTO:YBCO thin films grown under various deposition conditions on J_c and N-value anisotropy as well as the field dependence of the pinning force density, $F_p(H)$, at liquid nitrogen temperatures. We explain the appearance of symmetric shoulders in J_c (θ) and $N(\theta)$ by a matching effect which does not depend on the absolute magnitude of the applied magnetic field but rather on its c-component.

Results and Discussion

The growth of self-assembled nanocolumns is not only driven by interfacial energies and strain[34–36] but also by diffusion of the respective atomic species, which can be controlled by temperature[37–40], time (i.e. laser repetition rate)[41,13] and diffusion lengths (i.e. distances between deposited material). Furthermore, secondary phases[39] as well as growth direction (vicinality of the substrate)[42] influence the growth kinetics of nanocolumns.

In this study, films with various laser repetition rates f_{Dep} between 1/2 Hz and 50 Hz were grown at fixed (optimized) temperature in order to investigate the influence of different microstructures inside the BYNTO:YBCO matrix on the transport properties.

Microstructure

The YBCO matrix shows epitaxial growth on the STO substrates for all prepared films. As an example, Fig. 1 shows the Θ-2Θ scan for the film grown with a laser repetition rate of 1 Hz. For YBCO and BYNTO, just (00ℓ) and (00 2ℓ) peaks are visible, respectively. Y_2O_3 could be found by the appearance of its (004) peak and Y_2BaCuO_5 by its (220) peak. BYNTO nanoparticles are aligned cube-on-cube with the YBCO for all samples. This was confirmed by selected area electron diffraction (SAED) as well as pole figure measurements of YBCO (102) and BYNTO (220), Supp. Fig. S1. The intensity of the BYNTO (00ℓ) peaks and therefore the amount of biaxially incorporated BYNTO is increasing with decreasing f_{Dep} (Supp. Fig. S2). TEM cross section images of the films grown at 1 Hz (Fig. 2a,b and Supp. Fig. S4) and 5 Hz (Supp. Fig. S3) show three types of defects: BYNTO nanocolumns (horizontal), Y_2O_3 plates (vertical) and defects in the YBCO lattice like stacking faults (extra Y or CuO_2 planes) or anti-phase boundaries (APB). The density and morphology of the nanoparticles depend strongly on the laser repetition rate. With increasing f_{Dep} the density of the nanorods increases (1 Hz: 1 column per 29.9 nm, 5 Hz: 1 column per 14.5 nm), their diameter decreases (1 Hz: (10 ± 2) nm, 5 Hz: (8 ± 4) nm), and the density of Y_2O_3 plates seems to increase. Fig. 2c shows a large-area TEM cross section of 3200 nm width of the 1 Hz sample. Some of the nanorods seem to start or end within the film (red dots). However, if all columns are counted (black arrows plus red dots) an average column distance of $d = 29.9$ nm is calculated. This corresponds nicely to the value $d = 30.5$ nm obtained by plain-view TEM (Supp. Fig. S6). Therefore, we conclude that for f_{Dep} up to 5 Hz, most of the nanorods are penetrating the whole film and some are slightly inclined and cut by the lamella preparation. The components, BYNTO nanorods and Y_2O_3 particle, were further confirmed by EDX mapping of the contained elements (Supp. Fig. S5).

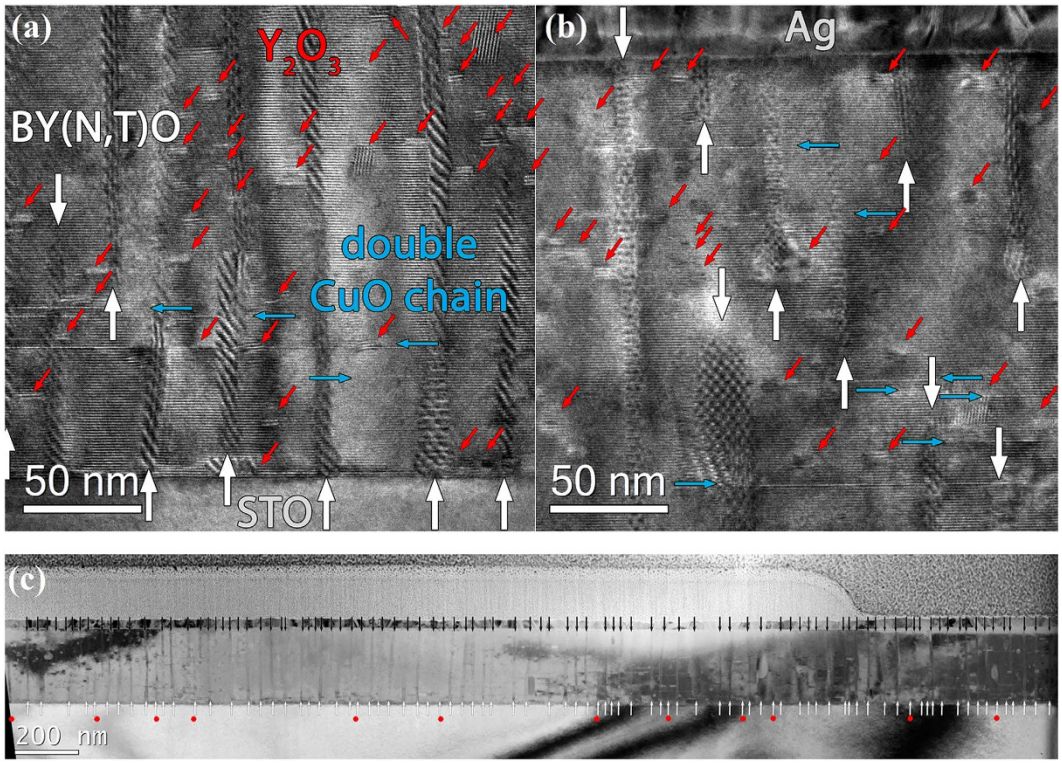

Figure 2. (**a**,**b**) HRTEM image of the 1 Hz sample at substrate-film interface (**a**) and near the film surface (**b**). Pinning centers such as BYNTO columns, Y_2O_3 particles and planar intergrowths are marked. (**c**) BFTEM cross section of the 1 Hz sample over an area of 3200 nm width. BYNTO columns are marked with arrows. Columns which are tilted (approx. 12% of them) are marked by red dots.

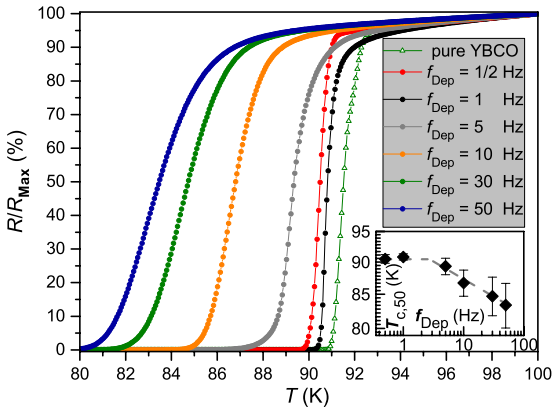

Figure 3. Relative resistance over applied temperature for BYNTO:YBCO films grown at laser repetition rates between 0.5 Hz and 50 Hz. Inset: Transition temperature versus laser repetition rate. Error bars indicate the transition width which was determined by taking the difference between $T_{c,90}$ and $T_{c,10}$.

Critical current density and Pinning force

Films grown at f_{Dep} of 1 Hz or 1/2 Hz show a transition temperature T_c of ~90 K, which is in the experimental range of undoped samples (90…92 K). In general, T_c decreases for higher repetition rates (Fig. 3), while the transition width ΔT_c (error bars in inset of Fig. 3) is increasing by a factor of 7 (ΔT_c (1 Hz) = 0.5 K, ΔT_c (50 Hz) = 3.3 K). The reduction in T_c might be avoidable by adjusting other PLD parameters such as deposition temperature, energy density, oxygen partial pressure and target-substrate distance. Whereas the samples with 1 Hz and 1/2 Hz are similar in their current carrying capability, the samples grown at 5 Hz or higher show much smaller J_c values at 77 K (Fig. 4a and Table 1). This reduction is mainly due to the reduced T_c value because the decrease in J_c is smaller at lower temperatures such as 30 K, Fig. 4b.

The critical current density in self field $J_{c,sf}$ at 77 K reaches values of 3.2 MA/cm^2 (1 Hz) and 4.0 MA/cm^2 (1/2 Hz) and decreases in an external field as it is expected for a high-temperature superconductors in the strong

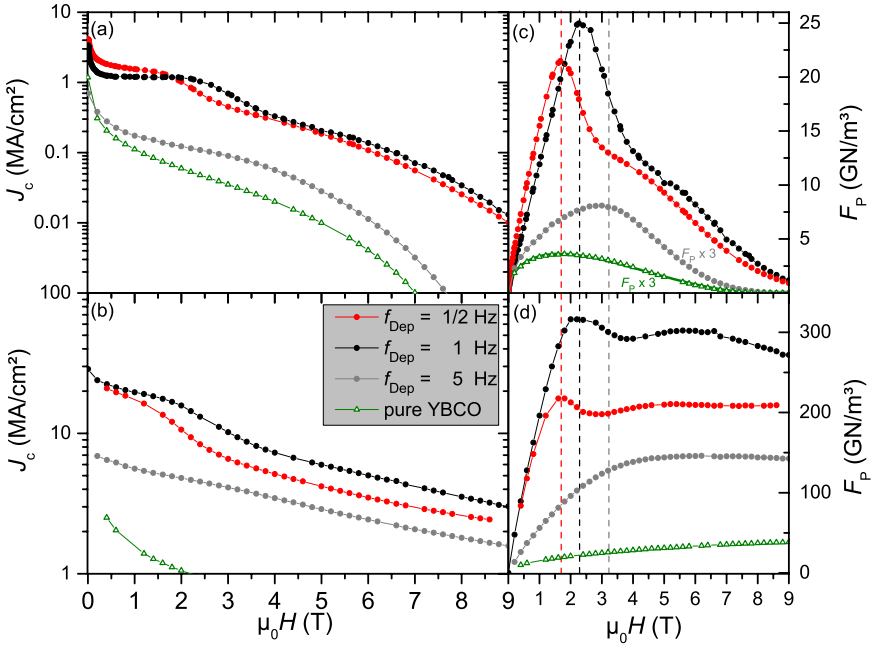

Figure 4. J_c versus applied magnetic field, $H \| c$, at 77 K (**a**) and 30 K (**b**) for the BYNTO:YBCO samples grown at 1/2 Hz, 1 Hz and 5 Hz as well as the corresponding F_P ($\mu_0 H$) at 77 K (**c**) and 30 K (**d**). The thickness of these films is around 250 nm. Green datapoints belong to a pure YBCO film without any additions. In this case F_P ($\mu_0 H$) at 77 K can be described with equation 1 (bold green line in (**c**), $p = 0.5$, $q = 2$).

f_{Dep}	$T_{c,50}$(K)	ΔT_c (K)	$J_{c,sf}$ (77K) (MA/cm²)	$\mu_0 H_{irr}$(T)	$F_{P,max}$ (77 K) (GN/m³)	B_{max} (T)	B_m^* (T)
0.5	90.5	0.7	4.0	10.5	21.5	1.6	2.0
1	90.8	0.5	3.3	11.2	25.0	2.3	2.7
5	88.1	1.3	0.7	8.7	2.7	3.2	–

Table 1. Overview of the superconductivity properties of the discussed films. ΔT_c was determined by taking the difference of $T_{c,90}$ and $T_{c,10}$, H_{irr} was estimated through the fit of equation (1).

pinning limit[43]. $J_{c,sf}$ values at 30 K as high as 28 MA/cm² can be achieved in BYNTO:YBCO films grown with laser repetition rates of 1 Hz or below. The critical current density is above 1 MA/cm² even for an external magnetic field of 9 T for all samples at this temperature (Fig. 4).The field dependence of J_c at 77 K shows an unusual behavior of samples with $f_{Dep} = 1$ Hz and 1/2 Hz (Fig. 4a and Supp. Fig. S7). Above approx. 500 mT, J_c stays almost constant for increasing fields.

The field dependence of the pinning force density is equally unusual. For these BYNTO:YBCO thin films, it is not possible to describe $F_P(H)$ by one Dew-Hughes function[44]

$$F_P \propto \left(\frac{H}{H_{irr}}\right)^p \left(1 - \frac{H}{H_{irr}}\right)^q \quad (1)$$

alone as it is possible for a YBCO film without any additions (bold green line in Fig. 4c). The field $B_{max} = \mu_0 H(F_{P,max})$ at which the maximum pinning force density is reached increases with laser repetition rate (1.6 T for 1/2 Hz, 2.3 T for 1 Hz and 3.2 T for 5 Hz). Similar $J_c(H)$ curves have recently been reported for $BaHfO_3$(BHO)-doped $SmBa_2Cu_3O_{7-\delta}$[45]. The pinning force density maximum for the 1 Hz sample (25 GN/m³ for the 250 nm thick film at 77 K), Fig. 4c, is among the highest values in YBCO at 77 K measured so far (e.g. 240 nm $BaSnO_3$-doped: 28.3 GN/m³[12], 500 nm BYNO-doped: 32.3 GN/m³ at 75.5 K[25], 200 nm $BaZrO_3$-doped: 21 GN/m³[17]). Other *RE*BCO films with slightly higher T_c values doped with BHO (370 nm GdBCO: 23.5 GN/m³[46], 300 nm SmBCO: 28 GN/m³[45]) show similar $F_{P,max}$ values at 77 K. The previously mentioned plateaus in $J_c(H)$ at 77 K also end at these fields B_{max}. Furthermore, B_{max} is temperature independent as can be seen by the dashed lines in Fig. 4c,d for the pinning force density at 77 K and 30 K (see also Supp. Fig. S8). Therefore, this plateau can be explained by a matching effect. Up to this field, every flux line can be pinned by an individual BYNTO column. The mean column distance of $d = 29.9$ nm, as observed in TEM for the 1 Hz sample, corresponds to a matching field B_m of approx. 2.3 T which corresponds quite well to the end position of the constant J_c region, respective peak position in $F_P(H)$, dashed black line Fig. 4c,d (2.3 T). This value was also confirmed by a TEM plain view image

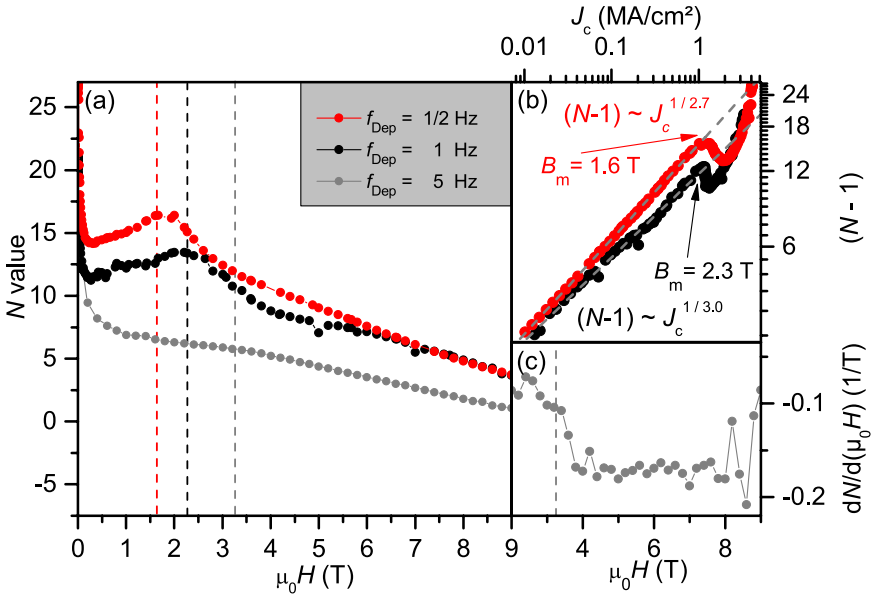

Figure 5. (**a**) *N*-value over field at 77 K for different samples. (**b**) J_c over *N* illustrating the reduced *N* values below B_m. (**c**) Derivation of the *N* value for the 5 Hz sample. B_m(5 Hz) is visible as step in the derivative.

where 312 columns are visible in a 0.289 μm² wide area which leads to a matching field of (2.23 ± 0.14) T (Supp. Fig. S6). The same correspondence between end of J_c plateau, B_{max} and B_m has been observed for BHO-doped $SmBa_2Cu_3O_{7-\delta}$/LAO[45] and $GdBa_2Cu_3O_{7-\delta}$/IBAD-MgO[46].

The *N* value

The electric field-current density characteristics $E(J)$ are well described by a power-law dependence, $E \sim J^N$, over a wide electric-field range in the vicinity of J_c. The *N* value has, in general, statistical and microscopic explanations. In inhomogeneous superconductors, $1/N$ is proportional to the variance in J_c as described by e.g. Warnes and Larbalestier[47] in statistical models. The good reproducibility of *N* and J_c in our measurements however points to a microscopic explanation for *N*. It has been shown by Griessen *et al.* that in high-T_c superconductors *N* is strongly influenced if not determined by flux creep processes. Here, the flux creep rate $S = \frac{d\ln M}{d\ln t} \sim \frac{1}{N-1}$ (M … magnetization)[48]. Strictly, this relation only holds if *S* and *N* are measured at the same electrical field *E*. In general, *N* values determined from creep rates (equation above) are larger than from magnetization measurements[49] and those are larger than determined from transport $E(J)$ curves[50] due to the negative curvature of $E(J)$ below the glass-liquid transition. For the considerations below, this effect can be ignored, however.

For flux creep processes determined by the pinning potential $U_0 \gg k_B T$ and under the assumption of a logarithmic *J*-dependence of U_0[51], $N = U_0/k_B T$ and, hence, $S = k_B T/U_0$ for $N \gg 1$ (i.e. neglecting a log. time dependence term). This in turn means that J_c, being determined itself by U_0, scales with *N*. This is indeed found on a variety of samples in a wide range of *N* values with an empirical relation $(N-1) \sim J_c^{1/p}$, $p \sim 3$, Fig. 5b. The origin of this power law is beyond the scope of this paper. As seen in Fig. 5, *N* is anticorrelated to J_c in a wide magnetic field region below the matching field. The explanation for this peculiarity is a second mechanism for flux creep effects. In the presence of strongly correlated 1D or 2D pinning centers and for $\mu_0 H < B_m$, the flux creep rate is determined by the ability of flux half loops and double kink structures to form and move between the pinning centers, which consequently leads to an effective "hopping" of the flux lines from nanocolumn to nanocolumn. The net velocity of the flux lines and so the creep rate depends on the probability of finding a free nanocolumn in the neighborhood. Since this probability decreases with increasing magnetic field $\mu_0 H < B_m$, *S* decreases and *N* increases for $\mu_0 H \rightarrow B_m$. This effect is the equivalent of a Mott insulator. As observed in magnetization measurements on irradiated YBCO single crystals with columnar defects[52], matching effects are only visible for a very narrow orientation distribution (splay) of the correlated defects, in that case of less than 4°. This, in turn, leads to an overall decreased J_c due to the increased creep rates. Larger splay values lead to lower creep rates and therefore higher J_c values but no observable matching effects. Similar reductions in creep rate due to additional defects in YBCO films have been reported recently for increased film thickness and substrate decoration[53], and nanoparticle addition (Y211, BZO, BYTO) in films grown by metall-organic deposition (MOD)[54,55]. In our samples, we observe high J_c values and matching effects. This is a consequence of the intermediate Y_2O_3 particles and stacking faults, which hinder the half loops and double kink structures from running parallel the nanocolumns and effectively jump to the next column[13].

Critical current density anisotropy

The anisotropy of the critical current density $J_c(\theta)$ at 77 K shows a maximum at 90° due to the electronic anisotropy of YBCO[56] and one at 180° due to *c*-axis correlated pinning[57] for all BYNTO:YBCO samples. Besides

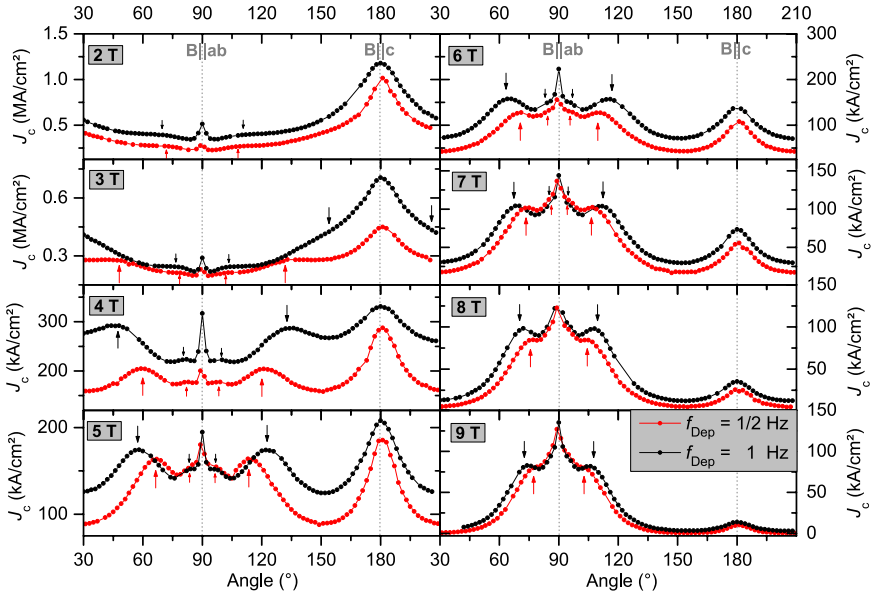

Figure 6. Anisotropy of the critical current density at 77 K at several fields for samples grown at low f_{Dep}, red 0.5 Hz and black 1 Hz. Large arrows indicate the position of the main off-axis maximum, where $B\cdot\cos(\theta)$ equals B_m^* (2.0 T for the red arrows and 2.7 T for the black arrows), small arrows indicate a second off-axis maximum.

these well understood features of $J_c(\theta)$ additional maxima are visible. They appear as pairs which are oriented symmetrically around the *c*-axis peak similar to the shoulder formation seen by Ercolano *et al.*[30] but more pronounced. The shoulder position with respect to the *c*-axis depends on the used laser repetition rate as well as the applied field, Fig. 6. Only the samples grown at a laser repetition rate of 1 Hz and 1/2 Hz will be discussed in the following. Because of the lower J_c values, the shoulders of the 5 Hz sample are barely visible. The appearance and the position of these shoulders becomes comprehensible if *N* value and J_c are plotted versus the *c*-axis component of the applied magnetic field, $B^c = \mu_0 H\cdot\cos(\theta)$, Fig. 7a,b. For both samples, the *N* value maxima (and hence minima in *S*) appear once B^c reaches the matching field B_m just the same as for J_c at $H\|c$. A similar effect has recently been observed by Trastoy *et al.*[58] on YBCO films with a periodic square pattern of artificial pin holes produced by ion irradiation. They have seen strong matching effects with $\mu_0 H\cdot\cos(\theta)$ in field and angular dependence of resistivity and glass-liquid transition, concurrent with an increased mass anisotropy due to partial deoxygenation and a 2D glass-liquid transition. Our results show that this type of matching is independent of dimensionality (our samples are 3D) and periodicity (the BYNTO nanocolumns show a certain degree of density variance).

As calculated by Paulius *et al.*[59] for correlated irradiation defects and described by e.g. Ercolano *et al.*[30] and Jha *et al.*[60] for nanocolumns, the vortex is not pinned by one column alone but rather by several columns through a staircase-like path for angles θ smaller than a certain trapping or accommodation angle[56]. The flux line segments in between the vortices are pinned by additional defects, such as Y_2O_3, stacking faults and antiphase boundaries, as observed in TEM. The specific position B_m^*, where the $J_c(\theta)$ curves have their maximum in $J_c(B^c)$ is slightly raised compared to the matching field and the maxima in the *N* value (2.0 T for $f_{Dep} = 1/2$ Hz and 2.7 T for $f_{Dep} = 1$ Hz, Fig. 7c,d). Apparently, the extrema in creep rate *S* and hence the *N* value are determined solely by the occupation of the *c*-axis aligned correlated defects. Therefore, they appear at the matching field B_m. Additional intermediate defects contribute to J_c for field directions closer to *c* and lead to a further increase in J_c in a small region of $B_m < B^c < B_m^*$. This region (shaded area in Fig. 7) shows again anti-correlation between *N* and J_c (i.e. creep rate *S* not determined by pinning potential U_0). However, this configuration is different from the case $H\|c$, since here the anti-correlation appears above B_m, whereas it appears below B_m for $H\|c$.

Besides the strongly pronounced shoulders, a second pair of shoulders can be seen for fields up to 8 T (Fig. 6, small arrows). They have a much smaller amplitude and their position is much closer to 90°. The position of those peaks does not scale with the *c*-axis component of the applied magnetic field, B^c. A possible scenario for those peaks might be a combined effect of fractional occupation of the correlated defects and anisotropic pinning of the flux line segments at intermediate extended defects. This has to be investigated in more detail in future studies.

Conclusion

BYNTO-doped YBCO films were successfully grown using different laser repetition rates. Only for sufficiently long diffusion times ($f_{Dep} = 1$ Hz or lower), very high critical current densities were achieved. All films have a rich microstructure consisting of pinning centers with different size, shape and orientation distribution. The interplay between strongly *c*-axis correlated BYNTO nanocolumns, *ab*-stacking faults, *c*-axis oriented APBs, atomic disorder and biaxially oriented but randomly distributed Y_2O_3 nanoparticles leads to additional new features in $F_P(H)$

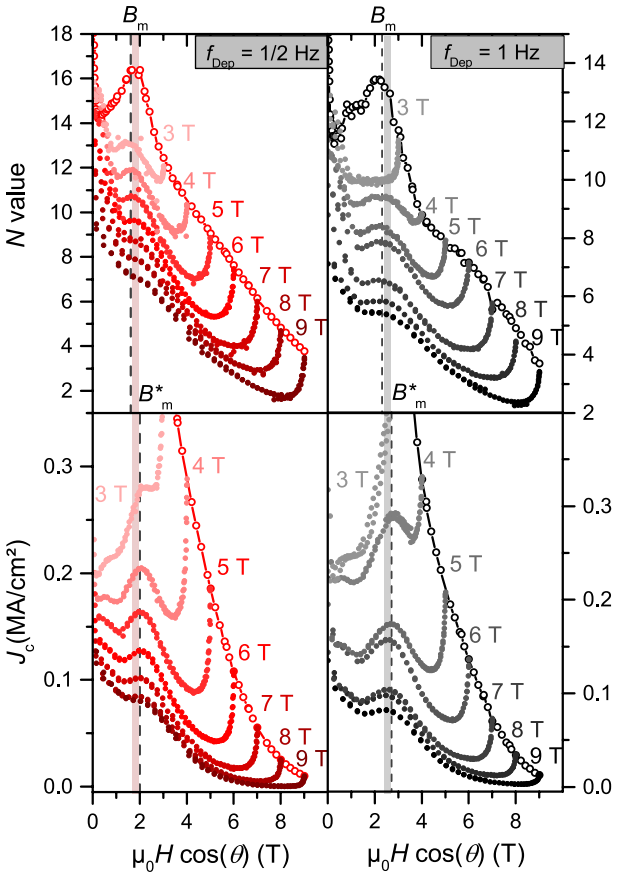

Figure 7. *N* value respectively J_c versus the *c*-axis component of the applied magnetic field B^c at 77 K. Open circles show the according data for $H \| c$. Shaded region $B_m < B^c < B^*_m$ indicates anti-correlation between *N* and J_c.

and $J_c(\theta)$. The critical current density shows almost constant values for magnetic fields up to several Tesla. The field where this plateau ends and where $F_P(H)$ has its highest value are equal to the matching field determined by TEM. A pinning force density of 25 GN/m^3 at 77 K at the matching field of 2.3 T was achieved for the film grown at 1 Hz, which is among the highest values reported for YBCO. At 30 K, deposition rates up to $f_{Dep} = 5$ Hz lead to critical current densities of more than 1 MA/cm^2 even in external fields of up to 9 T for $H \| c$.

The field dependence of the *N* value (the exponent of the $E(J)$ curves) and its scaling behavior with the corresponding J_c value clearly show different regions of flux depinning mechanisms, being dominated by the creation of half loop and double kink structures below the matching field and by usual flux creep processes due to weaker, uncorrelated, pinning centers above the matching field.

The anisotropy of the critical current density $J_c(\theta)$ as well as $N(\theta)$ are composed of two additional shoulder formations besides the maxima at 0° and 90° which appear at different angles if the applied magnetic field strength is changed. The existence of these shoulders can be explained by a staircase-like path of the vortices and additional pinning at intermediate defects. At a certain angle, the magnetic fields *c*-axis component $\mu_0 H \cdot \cos\theta$ reaches the matching field B_m which is accompanied by a maximum of the *N* value. Because of further contribution of intermediate defects to J_c but not to *N*, the maximum at the critical current density anisotropy B^*_m is slightly higher than the matching field B_m.

Due to their ability to grow as very uniformly sized, distributed and oriented nanocolumns, $Ba_2Y(Nb/Ta)O_6$ nano-precipitates in $YBa_2Cu_3O_{7-\delta}$ thin films are not only effective artificial pinning centers for increased J_c and F_P values but also a model system to study matching effects and flux creep.

Methods

BYNTO:YBCO films were prepared by pulsed laser deposition (PLD) using a YBCO target with 2.5 mol% BYNO and 2.5 mol% BYTO. The target was prepared by mixing the precursor oxides (barium oxide, yttrium oxide, tantalum oxide and niobium oxide) in the appropriate amount with YBCO powder and grinding the mixture in an agate mortar. The powder was pressed in pellets and sintered at 950 °C in flowing O_2 for 24 h. A Lambda Physics LPX305i KrF excimer laser ($\lambda = 248$ nm, $t_{pulse} = 25$ ns) was used with an energy density of 1.6 J/cm^2 at the target surface to grow BYNTO:YBCO films of approx. 250 nm thickness on single crystalline (100)-oriented $SrTiO_3$ (STO). An oxygen partial pressure of 0.4 mbar was maintained during the deposition process. The substrate temperature was set to 840 °C and checked with a HEITRONICS ceramic pyrometer. The laser repetition rate f_{Dep} was

varied between 0.5 Hz and 50 Hz. Oxygen loading of the YBCO films took place in 400 mbar O_2 for 1 hour at 770 °C. A silver cap layer of several nm thickness was deposited afterwards to improve the contact resistance.

Surface morphology and film thickness were analyzed by scanning electron microscopy using a JEOL JSM-6510 and an FEI Helios Nanolab 600i to cut cross sections by a focused gallium ion beam. Transmission electron microscopy (TEM) analysis was carried out on an FEI Osiris microscope, equipped with a 'Super-X' wide solid angle EDX detector, operated at 200 kV for bright field transmission electron microscopy (BFTEM), high angle annual dark field scanning transmission electron microscopy (HAADF STEM) and energy dispersive X-ray spectroscopy (EDX). FEI Titan 'cubed' electron microscope operated at 300 kV, equipped with an aberration corrector for the probe-forming lens as well as a high-brightness gun was used for high-resolution transmission electron microscopy (HRTEM). X-ray diffraction was carried out on a Bruker D8 Advance with a Co anode in a modified parallel-beam geometry for Θ-2Θ scans. Pole figures were measured at a Philips X'Pert PW3040 with a Cu anode in Bragg-Brentano geometry.

Bridges of 800 nm length and approx. 20 μm width for transport current measurements were prepared by laser cutting. Field and angular dependencies of critical current density J_c and exponent N of the $V(I)$ curves were measured in a four-point assembly in magnetic fields up to 9 T with a Quantum Design physical properties measurement system (PPMS). J_c was defined by an electrical field criterion of 1 μV/cm on $V(I)$ curves fitted as $E \sim J^N$ in the first decade of E above E_c. The angular dependence of the critical current density was measured under maximum Lorentz force configuration. To correct for small heating effects, the absolute value of some of those measurements were corrected to the value measured at $H \| c$ where thermal contact was better.

References

1. Foltyn, S. R. *et al.* Materials science challenges for high-temperature superconducting wire. *Nature Materials* **6,** 631–642 (2007).
2. Namba, M., Awaji, S., Watanabe, K., Nojima, T. & Okayasu, S. *c*-Axis-correlated pinning properties in heavy-ion-irradiated Y123 films. *Physica C* **468,** 1652–1655 (2008).
3. Aytug, T. *et al.* Enhanced flux pinning and critical currents in $YBa_2Cu_3O_{7-\delta}$ films by nanoparticle surface decoration: Extension to coated conductor templates. *J. Appl. Phys.* **104,** 043906 (2008).
4. Abellán, P. *et al.* Interaction between solution derived $BaZrO_3$ nanodot interfacial templates and $YBa_2Cu_3O_7$ films leading to enhanced critical currents. *Acta Mat.* **59,** 2075 (2011).
5. MacManus-Driscoll, J. L. *et al.* Systematic enhancement of in-field critical current density with rare-earth ion size variance in superconducting rare-earth barium cuprate films. *Appl. Phys. Lett.* **84,** 5329 (2004).
6. Miura, M. *et al.* Rare earth substitution effects and magnetic field dependence of critical current in $Y_{1-x}RE_x$ $Ba_2Cu_3O_y$ coated conductors with nanoparticles (RE = Sm, Gd). *Appl. Phys. Exp.* **2,** 023002 (2009).
7. Selinder, T. *et al.* Yttrium oxide inclusions in $YBa_2Cu_3O_x$ thin films: Enhanced flux pinning and relation to copper oxide surface particles. *Physica C* **202,** 69–74 (1992).
8. Xu, A., Jaroszynski, J., Kametani, F. & Larbalestier, D. Broad temperature range study of J_c and H_{irr} anisotropy in $YBa_2Cu_3O_x$ thin films containing either Y_2O_3 nanoparticles or stacking faults. *Appl. Phys. Lett.* **106,** 052603 (2015).
9. Mele, P. *et al.* High pinning performance of $YBa_2Cu_3O_{7-x}$ films added with Y_2O_3 nanoparticulate defects. *Supercond. Sci. Technol.* **28,** 024002 (2015).
10. MacManus-Driscoll, J. L. *et al.* Strongly enhanced current densities in superconducting coated conductors of $YBa_2Cu_3O_{7-\delta}$ + $BaZrO_3$. *Nature Materials* **3,** 439–443 (2004).
11. Hänisch, J., Cai, C., Hühne, R., Schultz, L. & Holzapfel, B. Formation of nanosized $BaIrO_3$ precipitates and their contribution to flux pinning in Ir-doped $YBa_2Cu_3O_{7-\delta}$ quasi-multilayers. *Appl. Phys. Lett.* **86,** 122508 (2005).
12. Mele, P. *et al.* Ultra-high flux pinning properties of $BaMO_3$-doped $YBa_2Cu_3O_{7-\delta}$ thin films (M = Zr, Sn). *Supercond. Sci. Technol.* **21,** 032002 (2008).
13. Maiorov, B. *et al.* Synergetic combination of different types of defect to optimize pinning landscape using $BaZrO_3$-doped $YBa_2Cu_3O_7$. *Nature Materials* **8,** 398–404 (2009).
14. Sieger, M. *et al.* $BaHfO_3$-doped thick $YBa_2Cu_3O_{7-\delta}$ films on highly alloyed textured Ni-W tapes. *IEEE Trans. Appl. Supercond.* **25,** 6602604 (2015).
15. Zhao, R. *et al.* Precise tuning of $(YBa_2Cu_3O_{7-\delta})_{1-x}$: $(BaZrO_3)_x$ thin film nanocomposite structures. *Adv. Funct. Mater.* **24,** 5240–5245 (2014).
16. Xu, A. *et al.* Strongly enhanced vortex pinning from 4 to 77 K in magnetic fields up to 31 T in 15 mol.% Zr-added (Gd, Y)-Ba-Cu-O superconducting tapes. *APL Materials* **2,** 046111 (2014).
17. Gutiérrez, J. *et al.* Strong isotropic flux pinning in solution-derived $YBa_2Cu_3O_{7-x}$ nanocomposite superconductor films. *Nat. Matter.* **6,** 367–373 (2007).
18. Miura, M. *et al.* Mixed pinning landscape in nanoparticle-introduced $YgdBa_2Cu_3O_y$ films grown by metal organic deposition. *Phys. Rev. B* **83,** 184519 (2011).
19. Erbe, M. *et al.* $BaHfO_3$ artificial pinning centres in TFA-MOD-derived YBCO and GdBCO thin films. *Supercond. Sci. Technol.* **28,** 114002 (2015).
20. Llordés, A. *et al.* Nanoscale strain-induced pair suppression as a vortex-pinning mechanism in high-temperature superconductors. *Nat. Matter.* **11,** 329–336 (2010).
21. Wimbush, S. C. *et al.* Interfacial strain-induced oxygen disorder as the cause of enhanced critical current density in superconducting thin films. *Adv. Funct. Mater.* **19,** 835–841 (2009).
22. Ercolano, G., Harrington, S. A., Wang, H., Tsai, C. F. & MacManus-Driscoll, J. L. Enhanced flux pinning in $YBa_2Cu_3O_{7-\delta}$ thin films using Nb-based double perovskite additions. *Supercond. Sci. Technol.* **23,** 022003 (2010).
23. AbduUah, M. & Tan, B. Superconducting properties of niobium-doped Y-Ba-Cu-Nb-O superconductors. *Sol. Stat. Comm.* **93,** 93 (1995).
24. Wee, S. H. *et al.* Formation of self-assembled, double-perovskite, Ba_2YNbO_6 nanocolumns and their contribution to flux-pinning and J_c in Nb-doped $YBa_2Cu_3O_{7-\delta}$ Films. *Appl. Phys. Express* **3,** 023101 (2010).
25. Feldmann, M. D. *et al.* Improved flux pinning in $YBa_2Cu_3O_7$ with nanorods of the double perovskite Ba_2YNbO_6. *Supercond. Sci. Technol.* **23,** 095004 (2010).
26. Ercolano, G. *et al.* Strong correlated pinning at high growth rates in $YBa_2Cu_3O_{7-x}$ thin films with Ba_2YNbO_6 additions. *J. Appl. Phys.* **116,** 033915 (2014).
27. Wee, S. H. *et al.* Enhanced flux pinning and critical current density via incorporation of self-assembled rare-earth barium tantalate nanocolumns within $YBa_2Cu_3O_{7-\delta}$ films. *Phy. Rev. B* **81,** 140503 (2010).
28. Holesinger, T. G. *et al.* Nanorod self-assembly in high J_c $YBa_2Cu_3O_{7-x}$ films with Ru-based double perovskites. *Materials* **4,** 2042 (2011).

29. Coll, M. *et al.* Solution-derived $YBa_2Cu_3O_7$ nanocomposite films with a Ba_2YTaO_6 secondary phase for improved superconducting properties. *Supercond. Sci. Technol.* **26,** 015001 (2013).
30. Ercolano, G. *et al.* State-of-the-art flux pinning in $YBa_2Cu_3O_{7-\delta}$ by the creation of highly linear, segmented nanorods of $Ba_2(Y/Gd)(Nb/Ta)O_6$ together with nanoparticles of $(Y/Gd)_2O_3$ and $(Y/Gd)Ba_2Cu_4O_8$. *Supercond. Sci. Technol.* **24,** 095012 (2011).
31. Siraj, K. *et al.* Enhanced self-field critical current density of nano-composite $YBa_2Cu_3O_7$ thin films grown by pulsed-laser deposition. *Europ. Phys. Lett.* **82,** 57006 (2008).
32. AwangKechik, M. *et al.* Artificial pinning centres in $YBa_2Cu_3O_{7-\delta}$ thin films by $Gd_2Ba_4CuWO_y$ nanophase inclusions. *Supercond. Sci. Technol.* **22,** 034020 (2009).
33. Reich, E. *et al.* Structural and pinning properties of $Y_2Ba_4CuMO_y$ (M = Nb, Zr)/$YBa_2CuO_{7-\delta}$ quasi-multilayers fabricated by off-axis pulsed laser deposition. *Supercond. Sci. Technol.* **22,** 105004 (2009).
34. MacManus-Driscoll, J. L. Self-assembled heteroepitaxial oxide nanocomposite thin film structures: Designing interface-induced functionality in electronic materials. *Adv. Funct. Mater.* **20,** 2035 (2010).
35. Wee, S. H. *et al.* Self-assembly of nanostructured, complex, multication films via spontaneous phase separation and strain-driven ordering. *Adv. Funct. Mater.* **23,** 1912 (2013).
36. Wu, J. Z. *et al.* The effect of lattice strain on the diameter of $BaZrO_3$ nanorods in epitaxial $YBa_2Cu_3O_{7-\delta}$ films. *Supercond. Sci. Technol.* **27,** 044010 (2014).
37. Kiessling, A. *et al.* Nanocolumns in $YBa_2Cu_3O_{7-x}$/$BaZrO_3$ quasi-multilayers: formation and influence on superconducting properties. *Supercond. Sci. Technol.* **24,** 055018 (2011).
38. Feldmann, D. M. *et al.* Influence of growth temperature on critical current and magnetic flux pinning structures in $YBa_2Cu_3O_{7-x}$. *Appl. Phys. Lett.* **91,** 162501 (2007).
39. Baca, F. J. *et al.* Interactive growth effects of rare-earth nanoparticles on nanorod formation in $YBa_2Cu_3O_{7-x}$ thin films. *Adv. Funct. Mater.* **23,** 4826 (2013).
40. Ichino, Y. *et al.* Determinant for self-organization of BaMO_3 nanorods included in vapor-phase-grown $RE$$Ba_2Cu_3O_y$ films. *IEEE Trans. Appl. Supercond.* **25,** 6604506 (2015).
41. Harrington, S. A. *et al.* Understanding nanoparticle self-assembly for a strong improvement in functionality in thin film nanocomposites. *Nanotechnology* **21,** 095604 (2010).
42. Baca, F. J. *et al.* Control of $BaZrO_3$ nanorod alignment in $YBa_2Cu_3O_{7-x}$ thin films by microstructural modulation. *Appl. Phys. Lett.* **94,** 102512 (2009).
43. van der Beek, C. J. *et al.* Flux pinning in $PrFeAsO_{0.9}$ and $NdFeAsO_{0.9}F_{0.1}$ superconducting crystals. *Phys. Rev. B* **81,** 174517 (2010).
44. Dew-Hughes, D. Flux pinning mechanisms in type II superconductors. *Phil. Magazine* **30,** 293–305 (1974).
45. Miura, S. *et al.* Vortex pinning at low temperature under high magnetic field in $SmBa_2Cu_3O_y$ superconducting films with high number density and small size of $BaHfO_3$ nano-rods. *Supercond. Sci. Technol.* **28,** 114006 (2015).
46. Awaji, S. *et al.* High-performance irreversibility field and flux pinning force density in $BaHfO_3$-doped $GdBa_2Cu_3O_y$ tape prepared by pulsed laser deposition. *Appl. Phys. Express* **8,** 023101 (2015).
47. Warnes, W. H. & Larbalestier, D. C. Analytical technique for deriving the distribution of critical currents in a superconducting wire. *Appl. Phys. Lett.* **48,** 1403 (1986).
48. Griessen, R. Relaxation effects, I–V curves and irreversibility lines in high-T_c superconductors. *Physica C* **315,** 175–323 (1991).
49. Yamasaki, H. & Mawatari, Y. Current-voltage characteristics of melt-textured YBCO obtained from the field-sweep rate dependence of magnetization. *IEEE Trans Appl. Supercond.* **9,** 2651 (1999).
50. Thompson, J. R. *et al.* Wide-range characterization of current conduction in high- T_c coated conductors. *Appl. Phys. Lett.* **93,** 042506 (2008).
51. Zeldov, E. *et al.* Flux creep characteristics in high-temperature superconductors. *Appl. Phys. Lett.* **56,** 680 (1990).
52. Niebieskikwiat, D. *et al.* Suppression of matching field effects by splay and pinning energy dispersion in $YBa_2Cu_3O_7$ with columnar defects. *Phys. Rev. B* **63,** 144504 (2001).
53. Miu, D. *et al.* Inhibition of the detrimental double vortex-kink formation in thick $YBa_2Cu_3O_7$ films with $BaZrO_3$ nanorods. *Supercond. Sci. Technol.* **26,** 045008 (2013).
54. Haberkorn, N. *et al.* High-temperature change of the creep rate in $YBa_2Cu_3O_{7-\delta}$ films with different pinning landscapes. *Phys. Rev. B* **85,** 174504 (2012).
55. Rouco, V. *et al.* Vortex creep in TFA–YBCO nanocomposite films. *Supercond. Sci. Technol.* **27,** 115008 (2013).
56. Blatter, G., Feigelman, M. Y., Geshkenbein, V. B., Larkin, A. I. & Vinokur, V. M. Vortices in high-temperature superconductors. *Rev. Mod. Phys.* **66,** 1125–1388 (1994).
57. Civale, L. *et al.* Angular-dependent vortex pinning mechanisms in $YBa_2Cu_3O_7$ coated conductors and thin films. *Appl. Phys. Lett.* **84,** 2121–2123 (2004).
58. Trastoy, J. *et al.* Unusual magneto-transport of $YBa_2Cu_3O_{7-\delta}$ films due to the interplay of anisotropy, random disorder and nanoscale periodic pinning. *New Journal of Physics* **15,** 103022 (2013).
59. Paulius, L. M. *et al.* Effects of 1-GeV uranium ion irradiation on vortex pinning in single crystals of the high-temperature superconductor $YBa_2Cu_3O_{7-\delta}$. *Phys. Rev. B* **56,** 913 (1997).
60. Jha, A. K. *et al.* Tailoring the vortex pinning strength of YBCO thin films by systematic incorporation of hybrid artificial pinning centers. *Supercond. Sci. Technol.* **28,** 114004 (2015).

Acknowledgements

The authors gratefully acknowledge J. Scheiter, U. Besold, and U. Fiedler for technical assistance. This work was financially supported by EUROTAPES, a collaborative project funded by the European Commission's Seventh Framework Program (FP7 / 2007-2013) under Grant Agreement no. 280432.

Author Contributions

L.O. and M.S. deposited the samples and conducted the electrical transport measurements as well as XRD, J.H. and R.H. designed the experiment, B.H. and L.S. supervised parts of the project, A.M. and G.V.T. prepared the TEM images, M.B. and J.L.M.D. devised the compositions and prepared the PLD targets, P.P. deposited the silver layer, R.N. prepared microbridges by laser cutting. The manuscript was prepared by L.O. and J.H. All authors took part in discussion and analysis of results and contributed to and reviewed the manuscript.

Additional Information

Supplementary information accompanies this paper at http://www.nature.com/srep

Competing financial interests: The authors declare no competing financial interests.

How to cite this article: Opherden, L. *et al.* Large pinning forces and matching effects in $YBa_2Cu_3O_{7-\delta}$ thin films with $Ba_2Y(Nb/Ta)O_6$ nano-precipitates. *Sci. Rep.* **6**, 21188; doi: 10.1038/srep21188 (2016).